Simulating droplet adhesion on superhydrophobic surfaces

Pawan Kumar* and Joseph D. Berry[†]
Department of Chemical Engineering, University of Melbourne, Parkville, Melbourne, 3010, Victoria, Australia
(Dated: November 27, 2025)

A numerical model is proposed to simulate the adhesion, compression, and subsequent detachment of a microliter droplet from a superhydrophobic surface composed of chemically homogeneous pillars arranged in a periodic fashion, replicating a typical force probe microscopy experiment. We observe that as the droplet is pulled away from the surface, the net vertical force varies in a typical sawtooth manner with peculiar peaks and troughs, characteristic of the surface. The force first reaches a maximum before the droplet detaches from the surface with a comparatively lower force. The force variation predicted by the numerical model is in good agreement with the experimental results of Kumar et al. [1]. We also studied the effect of evaporation on the variation in the adhesion force by simulating an evaporating droplet on a superhydrophobic surface. For an evaporating droplet, the numerically predicted maximum and detachment force magnitudes are in good agreement with those obtained experimentally when we take into account the change in the droplet weight as it evaporates. The proposed method will be useful for the quantitative analysis and design of a variety of superhydrophobic surfaces and will pave the way for more accurate surface characterization based on droplet adhesion force measurements.

I. INTRODUCTION

Since the discovery of the Lotus leaf effect [2], a variety of surfaces have been developed to cater to specific wetting applications, for example, superhydrophobic water repellent surfaces [3, 4], sticky superhydrophobic surfaces (SSHS) [5, 6], and Slippery Liquid-Infused Porous Surfaces (SLIPS) [7, 8]. These surfaces are used in many industrial and engineering systems, for example in anti-icing [9, 10], anti-fouling [11, 12], and drag reducing [13, 14] applications. Sticky superhydrophobic surfaces are used in energy harvesting [15, 16] and selfcleaning surfaces [17], while SLIPS are used in applications requiring high droplet mobility [18]. The key to the functioning of these surfaces is the ability to control the mobility of a liquid droplet in contact with the surface. When a droplet is placed on a superhydrophobic surface, the surrounding air is trapped within the surface crevices and partially supports the droplet. The droplet is in contact with the surface asperities only at certain places, and the smaller the number of these contact points, that is, the roughness area fraction (ϕ) , the higher the droplet mobility. The mobility of the droplets can be quantified by measuring the advancing contact angle (θ_a) and the contact angle hysteresis (CAH). High $\theta_{\rm a}$ (> 150°) and low CAH (< 10°) are often associated with high mobility [19–21] (with the exception of SLIPS and Slippery Omniphobic Covalently Attached Liquid surfaces (SOCAL) [22] that exhibit low θ_a and low CAH [21]).

Although CAH and receding contact angle characterize a superhydrophobic surface, the physical parameters of interest, such as the adhesion force (F) and the lateral friction force (F_{fric}) between the surface and the droplet, cannot be directly determined. For example, Furmidge's

equation [23] relates F_{fric} to the droplet parameters as

$$F_{\rm fric} = k\sigma_{\rm la}w\left(\cos\theta_{\rm r} - \cos\theta_{\rm a}\right),\tag{1}$$

where w is the width of the droplet, $\theta_{\rm r}$ is the receding contact angle and $\sigma_{\rm la}$ is the interfacial tension of the liquidair interface. k is a geometrical prefactor that depends on the shape of the droplet that must be assumed depending on the specific case [24]. McHale et~al. [25] used a solid-liquid friction law similar to solid-solid friction (Amonton's laws) to predict the friction force of droplets on different surfaces Gao et~al. [26].

The adhesion force between a droplet and a surface can also be indirectly inferred using the following equation [27],

$$F = (\pi R^2) \, \Delta p - 2\pi R \sigma_{\rm la} \sin \theta_{\rm r},\tag{2}$$

where R is the radius of the droplet base and Δp is the Laplace pressure difference across the liquid-air interface. Clearly, to relate the contact angle values to the adhesion or friction forces, additional parameters such as the droplet base radius, the Laplace pressure difference, and a proportionality constant (k) are also required. For this reason, direct force measurement is preferred when parameters such as adhesion or lateral friction forces are to be determined. In addition, Contact Angle Goniometry (CAG) [28, 29], which is the most widely used technique to measure contact angles, is less sensitive to changes in surface wettability compared to direct force measurements [30]. Other scenarios where direct force measurements may be preferred over CAG are discussed in [1] and in other relevant studies [30–32].

Direct force measurement can be broadly categorized into two approaches: (a) force probe microscopy [32–35] and (b) atomic force microscopy (AFM) [30, 31, 36]. Both methods operate on similar principles but differ in the size of the droplet used. Force probe microscopy employs millimeter-sized droplets [37–40], whereas AFM

^{*} kumar.pawan.cot@gmail.com

[†] berryj@unimelb.edu.au

uses droplets with diameters on the order of tens of micrometers [30, 31, 41, 42]. To measure the lateral friction force, in force probe microscopy, a millimeter-sized droplet is attached to the end of an elastic material (such as a glass capillary) with a known spring constant. The capillary deflects as the droplet moves relative to the surface. This deflection, measured via a laser or camera, is used to calculate the lateral friction force [40]. The velocity of the relative motion is adjustable, enabling friction force measurements as a function of velocity. To measure the adhesion force, the droplet is attached to a disk [32], ring [43] or the tip of a needle [44], and brought into contact with the surface using a motorized stage. A sensitive microbalance measures the force during the interaction between the droplet and the surface.

Both the lateral friction forces [39, 40, 45, 46] and the adhesion forces [32, 33, 43, 47, 48] depend on the surface topography and chemical nature. However, during lateral force measurement, the droplet is asymmetric with simultaneous advancing and receding interfaces. As a consequence the dynamics of the contact line (CL) are complex in comparison to adhesion force measurements, where the entire CL is either receding or advancing. In addition, the droplet wetting and spreading behavior on superhydrophobic surfaces is predominantly governed by the receding contact line dynamics as the advancing contact angle stays constant, approaching 180° [49–62] (Schellenberger et al. using inverted laser scanning confocal microscopy demonstrated this in [63]). Therefore, direct adhesion force measurement is the most suitable for analysis of superhydrophobic surfaces.

The majority of the work on studying the adhesion forces on superhydrophobic surfaces focuses on developing experimental techniques [30–43, 45–48] with relatively fewer analytical or numerical treatments. Butt [64] proposed a formalism to calculate the capillary forces between rough solids connected by a capillary bridge. However, surface roughness was treated statistically and the effect of pillar geometry was not considered. This model is extremely useful for understanding the physics of capillary bridge formation and the effect of surface roughness, but it cannot be directly used to predict forces between a droplet and a pillared superhydrophobic surface. Baret and Brinkmann [65] studied the stability of a droplet attached to a pipette in contact with a flat surface by solving the Young-Laplace equation [66], but the study was limited to flat surfaces only and cannot be used as such to analyze the adhesion on pillared surfaces. Sadullah et al. used Lattice Boltzmann (LB) simulations to model a Centrifugal Adhesion Balance (CAB) system [68] and predicted droplet detachment for a variety of surfaces. However, only the effect of the receding contact angle (θ_r) on the detachment force was studied without considering the variation of the force with time and the associated dynamics of the CL. Chen et al. [69] used LB simulations to calculate the adhesion forces between a pillared surface and a droplet studying the effect of the wetting transition between the Wenzel and Cassie-Baxter states,

although the variation of force (with time or the position of the platform on which the droplet is placed) and the effect of pillar area fraction on the droplet adhesion were not considered. Sudersan et al. [70] used energy minimization simulations to calculate the variation in the adhesion force between a droplet attached to the tip of a cantilever and a flat surface as the tip is moved away from the surface. To the best of our knowledge, there is no numerical model available in the literature that can simulate the variation in the adhesion force between a droplet and a pillared superhydrophobic surface, replicating a typical force probe or atomic force microscopy experiment.

In this work, we present a novel numerical method to simulate the force probe microscopy using a microliter droplet on a superhydrophobic surface composed of cylindrical pillars arranged in a square pattern. We used this model to calculate the variation in the adhesion force as a function of time and compare it with the experimental results presented in [1]. The numerical model can simulate both force probe and atomic force microscopy. hereafter referred to as droplet probe microscopy. In addition, we also discuss the effect of evaporation on the variation in the adhesion force on superhydrophobic surfaces by simulating an evaporating droplet. Although cylindrical pillars arranged in a square pattern are considered in this work, the model is valid for arbitrary pillar geometries and distributions. The numerical model presented is useful for predicting the adhesion force on a variety of superhydrophobic surfaces and can also be used to develop a drop probe microscopy tool for surface characterization, as shown in [1].

II. PHYSICAL SYSTEM AND THE NUMERICAL MODEL

In this section, we discuss the approach for simulating the variation in net vertical force between a microliter droplet and a superhydrophobic surface composed of micrometer-sized pillars, capturing a typical droplet probe microscopy experiment. The volume of droplets used in this study is small; therefore, the Bond number for the system $Bo = \rho g R_d^2/\sigma_{\rm la}$, where ρ is the liquid density, g is the acceleration due to gravity and R_d is the radius of the droplet, is much smaller than unity. For example, for a 1.6 μ L water droplet in air, $Bo = 0.07 \ll 1$. Hence, the effect of gravity has been neglected in the present study. Although we discuss the method in the context of a millimeter sized droplet, the approach can be used to simulate smaller droplets as long as the surface roughness length scale $l_c \ll R$. The dynamics of the system are simulated as a series of equilibrium droplet morphologies (see [71] for details on the method) obtained by minimizing the total free energy of the droplet. The physical model is presented first followed by the numerical method used to capture the physics.

A. Physical Model

In a typical droplet probe microscopy experiment, a small droplet is attached at the end of a disk, a needle, or a cantilever (Fig. 1). The droplet is fixed relative to the disk but can move with the disk relative to the surface, which is kept on a movable or stationary stage. The entire process comprises five key stages, namely approach, snap-in, advance, recede, and detach, as depicted in Fig. 1a. During the approach stage, the droplet is brought closer to the surface either by moving it downward or by moving the surface upward via a movable stage. In the simulation, we model droplet/surface interaction by the downward and upward movement of the disk during the advance and recede stages, respectively. When the droplet first contacts the surface, it wets the top of the contact pillar, forming a CL that is pinned at the top edge of the pillar. The spread of the droplet on the top of the pillar takes place at a relatively fast capillary speed $(v_{\rm CV})$, which is roughly 1.6 m/s for the water-air system (and surface roughness of the order of approximately 10 μ m) [72]. This rapid movement of the interface is the *snap-in*. As the stage continues to move, the droplet gets compressed and the interface moves radially outward, wetting the tops of more pillars. The advancement of the CL over the surface is the advance stage. At the start of the recede stage, the movement of the disk is reversed. This results in a receding of the interface that culminates in the detachment of the droplet, which is the *detach* stage.

The total interfacial energy (E') of the system changes as the droplet moves through these stages. During the approach stage,

$$E' = \sigma_{la}A_{la} + \sigma_{sl}A_{disk} + \sigma_{sa}A_{surf}, \tag{3}$$

where σ_{la} , σ_{sl} , σ_{sa} are the interfacial tension of the liquidair, solid-liquid [73], and solid-air interfaces, respectively, A_{la} is the area of the liquid-air interface, A_{disk} is the area of the disk which is in contact with the droplet, and A_{surf} is the total surface area of the pillared surface. When the droplet contacts the surface (snap-in), a portion of the liquid-air interface is converted into the solid-liquid interface, while the same amount of solid-air interfacial area is removed. The total interfacial energy of the system when the droplet is in contact with the surface can be written as

$$E' = \sigma_{la}A_{la} + \sigma_{sl}A_{disk} + \sigma_{sl}A_{wet} + \sigma_{sa}A_{dry}, \quad (4)$$

where A_{wet} and A_{dry} are the wet and dry areas of the pillared surface ($A_{\text{dry}} = A_{\text{surf}} - A_{\text{wet}}$). Rearranging Eq. (4),

$$E = \sigma_{\rm la} \left(A_{\rm la} - \cos \theta_{\rm e} A_{\rm wet} \right). \tag{5}$$

Here $E = E' - \sigma_{\rm sl} A_{\rm disk} - \sigma_{\rm sa} A_{\rm surf}$ and $\theta_{\rm e}$ is the equilibrium contact angle, which is equal to the Young angle for an ideal (perfectly flat and chemically homogeneous)

surface. Since $\sigma_{\rm sl}$, $\sigma_{\rm sa}$, $A_{\rm disk}$, and $A_{\rm surf}$ are constants for a particular system, the change in the interfacial energy based on $E^{'}$ or E is the same. Henceforth, we use E to calculate any changes in the interfacial energy of the system. During each stage, the droplet takes a shape for which it has a minimum energy (Eq. (5)). During the advance and recede stages, the CL advances and recedes on the surface respectively, and therefore $A_{\rm wet}$ increases and decreases respectively. $A_{\rm wet}$ is zero when the droplet has not yet contacted the surface and when the droplet has detached from the surface (assuming that no micro-droplets are generated). For the intermediate states, $A_{\rm wet}$ changes depending on the position of the CL on the surface.

We now discuss the CL dynamics during the advance and recede stages. When the droplet contacts the surface (snap-in), the CL spreads on top of the pillars at capillary velocity until it is pinned to the edges of the pillar. If the disk is moved at an infinitesimally small velocity, the droplet is in equilibrium at every point in time. Therefore, the droplet takes a shape for which it has minimum total energy (Eq. (5)) and the CL is pinned to the edges of the pillar satisfying the boundary condition of Young's angle, that is, $n_s \cdot n_{la} = \cos \theta_e$. Here, n_s and n_{la} are the unit normal vectors for the solid surface (directed outward) and the liquid-air interface (directed towards the air), respectively. Following the solution of the Euler-Lagrange equation under a constant volume constraint (see de Gennes et al. [74] pp. 29-30), the liquid-air interface is a surface of constant mean curvature. This means that the total curvature (κ) at every point on the interface is the same, that is, $\kappa = \kappa_1 + \kappa_2 = c$. Here, κ_1 and κ_2 are the principal curvatures in the vertical (meridional) and horizontal (azimuthal) planes respectively (see Fig. 1a), and c is a constant depending on the position of the disk relative to the surface. As the disk moves further downward after snap-in, the CL pinning results in an increase in the meridional curvature, and a corresponding decrease in the azimuthal curvature, that continues until the interface contacts a new set of pillars in the direction of advancement. Subsequently, the CL forms on the new set of pillars and the droplet acquires a new equilibrium morphology. Therefore, the CL advances in a rolling motion, bending towards and then touching a new set of pillars in the advancement direction [63].

During the recede stage, the disk is moved in the opposite direction, gradually pulling the droplet away from the surface. Because of the pinning of the CL, the meridional curvature of the droplet decreases, and along with it the Laplace pressure inside the droplet also decreases. When the droplet cannot exist in equilibrium for a given disk position and CL shape, the CL executes a jump and pins on a new set of pillars in the direction of droplet receding. The equilibrium states just before and after the CL jump are the first and second critical states [71]. The stability of the CL is governed by the microscale interface dynamics, which is discussed in [1]. Upon subsequent travel of the disk, when the droplet cannot remain

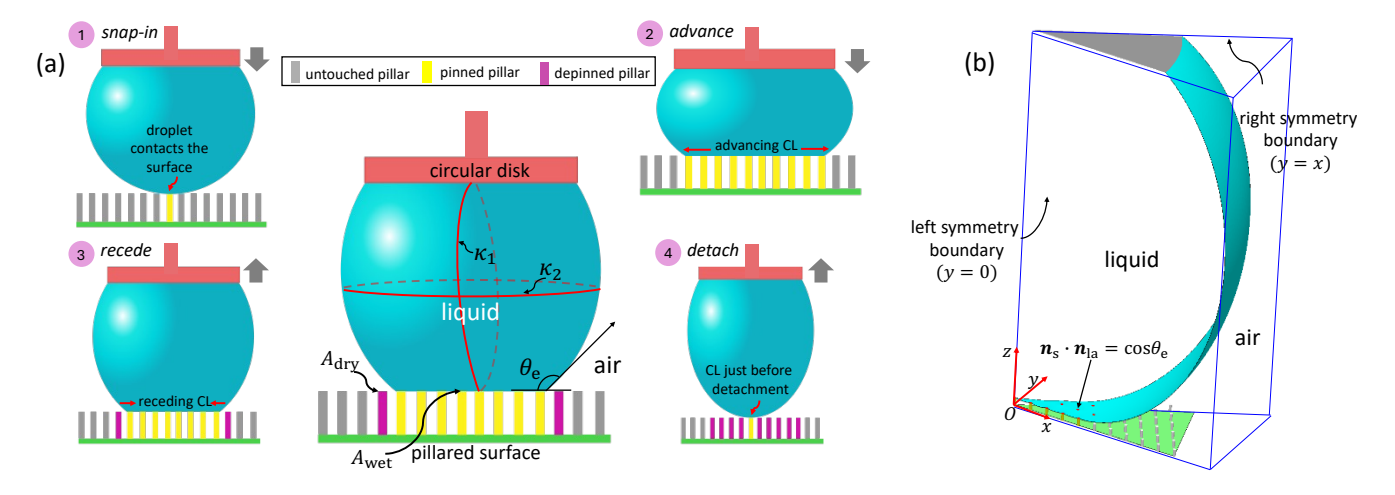


FIG. 1. (a) Pictorial representation of a typical droplet probe microscopy simulation. The method is depicted in 4 key steps (approach stage is not shown here): (1) Snap-in - the droplet contacts the surface, (2) Advance - the droplet is pushed against the surface by lowering the disk, (3) Recede - the droplet is pulled away from the surface by moving the disk in the opposite direction, and (4) Detach - the droplet detaches from the surface. (b) Schematic of the simulation domain. Due to symmetry, only one-eighth of the full droplet is simulated to reduce the computational time. The pillars in contact with the droplet are shown in yellow, the pillars from which the CL has depinned are shown in magenta and the pillars untouched by the liquid are shown in gray/white colors. Symmetry boundary conditions is applied on the left and right walls of the domain. Young's angle boundary condition is applied at the contact line. In equilibrium, the droplet maintains the condition of Young's angle boundary condition at the CL and the liquid-air interface being a surface of constant mean curvature ($\kappa_1 + \kappa_2$ being constant).

in equilibrium while attached to the surface for a particular disk position, the droplet detaches from the surface (detach stage).

B. Numerical model

In this section, we present the numerical model for simulating droplet probe microscopy discussed in §II A. We use the open-source software Surface Evolver (SE) [75] to implement the model. SE is a numerical optimization tool that works on the principle of gradient descent. To obtain equilibrium droplet morphologies, we use SE to minimize the total energy as given in Eq. (5). More details on the operation of SE can be found in the software manual [76].

Fig. 1b shows the computational domain used in the present study. Due to the inherent symmetry of the system, we simulate only an octant of the full droplet. A small droplet of a few microliters in volume is attached to a circular disk (a few millimeters in diameter) that can move in the z direction with the disk. The bottom surface of the domain is superhydrophobic, composed of cylindrical pillars of diameter d and height h (h/d = 2.0) arranged in a square pattern with an inter-pillar spacing $d_{\rm avg}$. The droplet-disk contact is constrained by a level-set constraint ($x^2 + y^2 - R_{\rm disk}^2 = 0$) that keeps the droplet pinned to the edges of the circular disk (with radius $R_{\rm disk}$). Young's angle boundary condition is applied at the CL. The symmetry boundary condition is applied to the left wall (y = 0) and the right wall (y = x) of the domain. Cylindrical pillars are generated using three-

dimensional shapes known as superquadrics [77] represented by the following equation:

$$\left(\frac{x-x_0}{r}\right)^2 + \left(\frac{x-x_0}{r}\right)^2 + \left(\frac{z}{h}\right)^n = 1.$$
 (6)

The parameter n controls the sharpness of the edge and the coordinates (x_0, y_0) define the location of the pillars on the surface. The constants r and h are the radius and height of the pillars, respectively. In this work, we use n = 250 to model pillars with smooth edges as representative of real surfaces.

III. CAPTURING INTERFACIAL DYNAMICS

In this section, we discuss the numerical approach to simulate the advancing and receding of the CL during the advance and recede stages, respectively. The approach used here is similar to the incremental advance approach proposed by Kumar and Harvie [71], with the difference being that instead of a portion of the interface, the entire droplet is simulated.

A. Snap-in and advance stages

Fig. 2 shows the simulation snapshots showing the *snap-in* and *advance* stages. The flow chart of the algorithm used to simulate these stages is shown in Fig. S1 in the Supplemental Material. The simulation starts with a droplet of a given volume attached to the disk.

The droplet is then gradually lowered until it contacts the pillar tops. The z coordinate of the lowest facet of the droplet (average of the three vertices of the facet) is tracked to determine the precise instant of contact. When the droplet contacts the surface, the intersection between the liquid-air mesh and the pillar mesh is obtained. The intersecting facets (and edges and vertices) of the interface are then constrained to lie on the pillars using Eq. (6). To account for the change in the total energy of the system, the interfacial tensions of the intersecting facets are changed from σ_{la} to $-\sigma_{la}\cos\theta_{e}$. This change in the interfacial tension signifies the change in the type of interface from the liquid-air interface to the solid-liquid interface. An equilibrium morphology of the droplet is obtained by subsequent energy minimization and mesh refinements (see §S7 in SI of [71]), which represents the droplet morphology at *snap-in*.

To advance the droplet, the disk is moved towards the surface by a small amount (δH) . With gradual minimization and mesh refinements, the equilibrium droplet morphology is obtained for the new position of the disk. To track the CL advancement, the regular gradient descent iteration in SE ('g') is replaced by a modified iteration step ('gadv'). In addition to the default gradient descent step, the 'gady' command also tracks the vertical position (z coordinates) of the vertices of the liquid-air interface whose projection on the x-y plane lies within the perimeter of the top of a pillar. When the liquidair interface approaches a pillar, 'gadv' places the liquidair facets (and edges and vertices) whose projection lies within the perimeter of the pillar top on the constraint of that pillar (Eq. (6)). The interfacial energies of the newly constrained liquid-air interface are also changed to $-\sigma_{\rm la}\cos\theta_{\rm e}$ to accommodate the changes in total energy of the system. The energy minimization is performed to obtain the equilibrium droplet morphology corresponding to the new position of the disk, and at the same time the intersection of the liquid-air interface pillars is monitored to advance the CL. This process is repeated until the disk travels a pre-determined distance or the force exerted on the surface by the droplet reaches a certain pre-determined maximum value. We use the principle of virtual work using Lagrange Multipliers (see [76] pp. 242-243) for calculating the adhesion force from equilibrium droplet morphologies (also see §S1 in the Supplemental Material).

B. Recede and detach stages

At the end of the advance stage, the droplet is in a compressed state between the disk and the surface. To recede the droplet, the disk is moved away from the surface in small steps (δH) followed by subsequent steps of energy minimization and mesh refinement (see snapshots in Fig. 2). The flow chart of the algorithm used to simulate these stages is shown in Fig. S2 in the Supplemental Material. The key during the recede stage is to

predict the CL depinning. The CL pinning at the edges of a pillar is governed by the Gibbs criterion [78], and the depinning starts when the local contact angle at any location on the pillar falls below θ_e [58, 79, 80]. Different approaches have been proposed in the literature to model the dynamics of receding CL, notably the stickslip motion, where the CL sticks to the trailing (towards the air side) [81] or leading (towards the liquid) [82] edge of the pillar before executing a jump. Yeong et al. [83] showed experimentally that the receding CL follows a slide-stick motion where it travels a small distance on the tops of the pillar moving towards the leading edge before executing a jump. Because we can only consider the equilibrium droplet morphologies, we cannot capture CL movement on the tops of the pillar. In the SE model, a modified iteration command 'grec' is used instead of the regular gradient descent command ('g'). This command computes the local contact angle (θ_{local}) at every point around the perimeter of each pillar on the CL and initiates the CL depinning from a pillar if $\theta_{local} \leq \theta_e$ at any point on the CL on that particular pillar. The CL depinning in the model is achieved by removing the pillar profile constraint (Eq. (6)) from the pinned vertices (and facets and edges) and changing the interfacial tension of the pinned facets from $-\sigma_{la}\cos\theta_{e}$ back to σ_{la} . This ignores any micro-droplet generation during CL receding [84], which is an acceptable assumption since changes in total interfacial energy due to loss of a small droplet volume can be neglected. After the CL depins from a pillar, subsequent energy minimization and gradual mesh refinements were performed to find the equilibrium droplet morphology. If the equilibrium droplet cannot be obtained under the given disk position and the CL position on the surface, the droplet detaches from the surface, indicating the detach stage.

The model outlined above assumes zero inherent hysteresis, that is, the CAH exhibited by the superhydrophobic surface is due to the presence of microscopic pillars only. It assumes that the parent surface is free from hysteresis, and the inherent advancing ($\theta_{\rm A}$) and receding $(\theta_{\rm R})$ contact angles are the same, that is, $\theta_{\rm A} = \theta_{\rm R} = \theta_{\rm e}$. However, in reality, there is always a finite inherent hysteresis present in the system, i.e. $\theta_{\rm A} > \theta_{\rm R}$, due to the presence of roughness at length scales below the primary roughness length scale (ie, below the pillar size and spacing). To consider the effect of inherent CAH in the numerical model, we take θ_A and θ_R instead of θ_e during the advance and recede stages, respectively (see [85] and [71] for a similar approach). However, the use of θ_R instead of $\theta_{\rm e}$ during the receding stage poses a numerical problem, especially if $\theta_{\rm R} < 90^{\circ}$. The error manifests itself as a wetting transition from the Cassie-Baxter to Wenzel state if the pillars are sparsely positioned and/or the inherent receding angle is too low. This wetting transition is nonphysical since the CL has to advance down the sides of the pillars, which will only happen if the local contact angle is greater than or equal to the inherent advancing angle [86]. To avoid this nonphysical behavior, either a

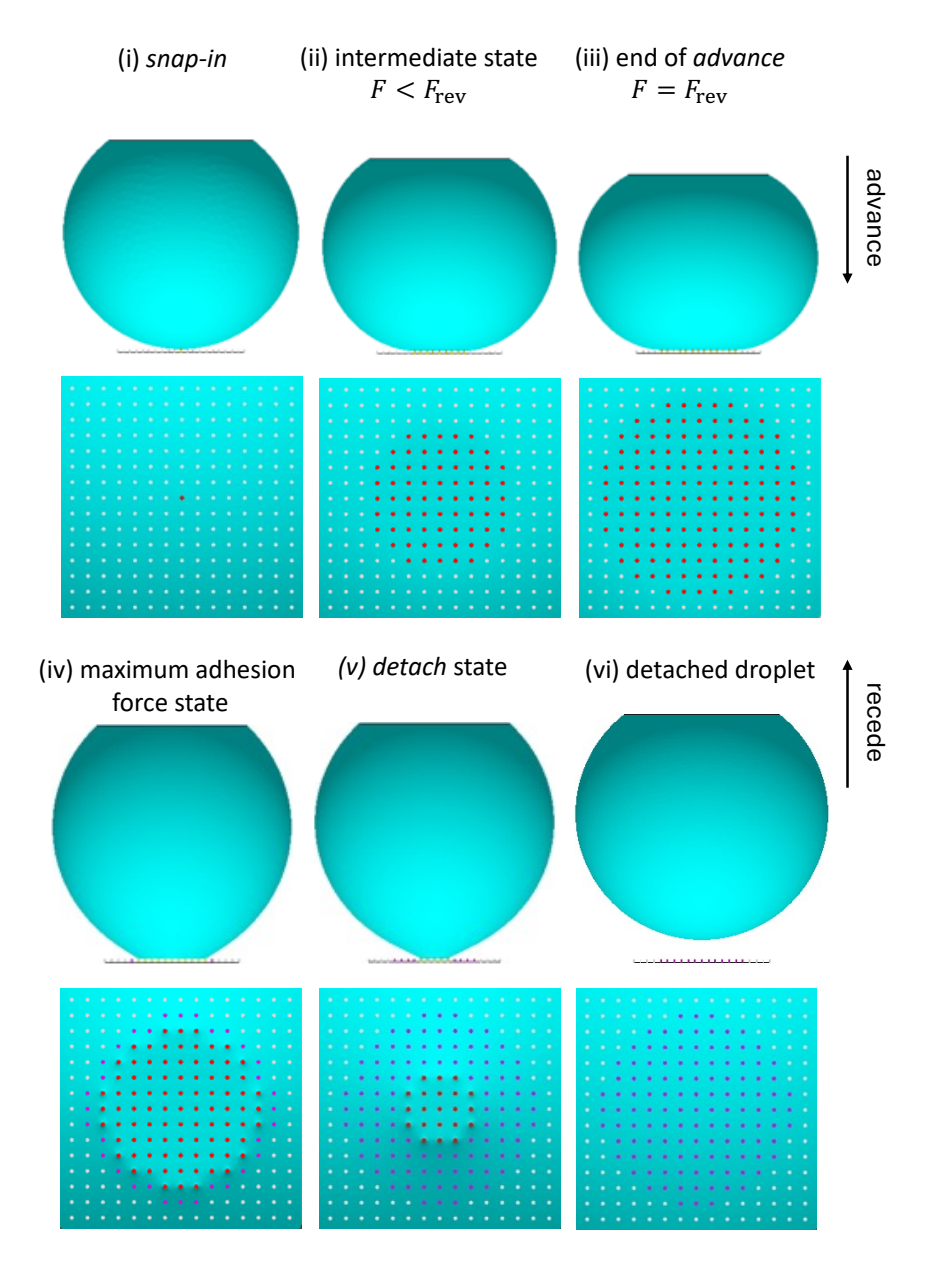


FIG. 2. Front and bottom view of the equilibrium droplet morphologies during the advance and recede stages obtained via numerical simulation on a superhydrophobic surface with $\theta_{\rm A}=111.2^{\circ}$, $\theta_{\rm R}=98.7^{\circ}$ and $\phi=0.05$ and a droplet of volume V=1.6 $\mu{\rm L}$. In the bottom view of the droplet the red, magenta and white colors are used to indicate the pillar tops in contact with the liquid, pillar tops where the CL has depinned and the pillar tops which were not in contact with the liquid at any point of time during the entire process, respectively. The high curvature of the liquid-air interface lying between the pillars can be seen in the bottom view of the equilibrium morphologies during the recede stage.

one-sided constraint could be applied to the CL vertices (see §3.6 in the manual [76]) or the vertices of the solid-liquid interface could be fixed (the approach used in this study) as shown in the algorithm flow chart in §S2 in the Supplemental Material.

IV. RESULTS

In this section, we present results for typical droplet probe microscopy simulated by the energy minimization approach discussed in §III. We discuss the variation in droplet and CL morphologies, and the forces that act between the droplet and a surface as the droplet contacts, advances, recedes, and then detaches from it. The surface considered is a superhydrophobic surface with microscopic cylindrical pillars with an aspect ra-

tio (height/diameter) of 2.0 and inherent advancing and receding contact angles of $\theta_{\rm A}=111.2^{\circ}$ and $\theta_{\rm R}=98.7^{\circ}$, respectively. These values are based on the complementary experimental study conducted in [1]. The simulations were performed in non-dimensional form using a characteristic length scale $l_0=10~\mu{\rm m}$ and a characteristic surface tension of $\sigma_0=72.8~{\rm mN/m}$. A droplet of volume, $V=1.6~\mu{\rm L}$ was used to generate the results. In non-dimensional form the pillars have a diameter of 1, height of 2, and the droplet has a volume of 1.6×10^6 .

A. Droplet and contact line morphology

Fig. 2 shows the equilibrium morphologies of a droplet during a typical droplet probe microscopy simulation. The footprint of the droplet is also shown in the figure capturing different stages of the simulation. We observe that the CL is non-continuous but discrete, lying on individual pillars that enclose the solid-liquid interfacial area, which is shown in red in the figure. Therefore, the conventional definition of the CL as the continuous line bounding the solid-liquid interface cannot be used for the Cassie-Baxter wetting state. To aid discussion, we adopt the concept of an apparent CL as previously described in the literature, defined as the intersection of the liquid-air interface with a plane parallel to the general surface and a certain distance from the tops of the pillars (Δz) . This definition is similar to the definition adopted by Dorrer and Rühe [52], and is discussed in detail in [1].

Fig. 3a shows the equilibrium interfacial morphologies that capture the microscale dynamics of the interface during a typical advance stage. We observe that the liquid-air interface curves until it touches a new pillar, at which instant the CL advances [63]. Fig. 3b shows the liquid-air interface on the x-z plane capturing the advancing motion. The dotted lines represent the interfacial morphology when the CL is pinned onto a set of pillars, and the solid line represents the equilibrium morphology just after the CL advancement. Due to the particular square arrangement of the pillars on the surface, the distance between the pillars along the $\psi = 0^{\circ}$ direction (d_{avg}) is smaller than that along the $\psi = 45^{\circ}$ direction $(\sqrt{2}d_{\text{avg}})$. Here, the angle ψ defines the direction of interfacial motion relative to the x axis. Therefore, the CL advances preferably in the $\psi = 45^{\circ}$ direction, resulting in a non-circular CL shape. Fig. 3c shows the evolution of the apparent CL ($\Delta z = 1 \,\mu\text{m}$) during the advance stage. The first (equilibrium state just before the interface touches the next pillar(s) in the advancing direction) and second (equilibrium state when the interface has just contacted a new pillar(s) in the advancing direction) critical states are shown as black and red curves, respectively. The CL starts as a circle (t_0) and slowly transforms into a shape that resembles an octagon as it advances (t_3) . During the advance stage, the microscale deformations in the liquid-air interface are contained in a very narrow region around the actual CL. Therefore, we

only see distortion of the apparent CL when measured close to the pillars ($\Delta z = 1~\mu \text{m}$). In Fig. 6a in Appendix A, we show that the apparent CL preserves a circular shape when measured sufficiently away from the pillars ($\Delta z = 20~\mu \text{m}$).

The dynamics of CL during the recede stage, unlike the rolling motion observed in the advance stage, can be described by a *stick-slip* motion [63, 80, 83]. The CL moves by executing occasional jumps between the first and second critical states, for example $i \to ii$ and $iii \to iv$ in Fig. 3d. Most of the time, the CL is pinned onto the pillars, while the interface continues to move macroscopically. This introduces large deformations in the liquidair interface in a microscopic region close to the CL (see Fig. 3f). These interfacial deformations result in a highly distorted CL during the recede stage. Fig. 3e shows the apparent CL ($\Delta z = 1 \, \mu \text{m}$) corresponding to the first (i and iii) and the second (ii and iv) critical states shown in black and red, respectively, in Fig. 3d. The receding CL morphology is more complex compared to that during the advancing motion due to the highly distorted liquid-air interface near the CL. However, as the distance from the pillars is increased, the interfacial deformations decrease and the apparent CL takes a less distorted shape. This is shown in Fig. 6b in Appendix A, where the apparent CL at $\Delta z = 20 \ \mu \text{m}$ is shown during the recede stage on a surface with $\phi = 0.05$. Interestingly, when sufficiently away from the pillars, such as $\Delta z = 20 \ \mu \text{m}$ as shown in Fig. 6b, the apparent receding CL starts from a shape that resembles an octagon and ends up appearing as a circle just before detachment. This is opposite to the evolution of the apparent CL during advance stage from a circle to that resembling an octagon. This evolution of the CL shape is due to the anisotropic nature of energy dissipation during interfacial dynamics [71]. The details of the CL dynamics, as well as the associated dissipation of energy and its relationship to contact angle hysteresis can be studied using the presented model, but are out of the scope of this study.

B. Adhesion force

In this section, we discuss the variation in the net vertical force (F) between the droplet and the surface during a typical droplet probe microscopy (see §S1 in the Supplemental Material for the numerical scheme for the calculation of force). Fig. 4a shows the variation in F with time in simulation units (assuming a unit disk velocity). A small drop in F is observed when the droplet contacts the surface, that is, the snap-in stage. This is due to the sudden drop in energy as the rapidly moving CL dissipates energy [87–91]. As the CL advances (the disk moves downward), F appears to increase linearly. However, a closer look reveals a sawtooth variation in the force during the advance stage. Every time the interface contacts a new set of pillars and the CL advances, there is a drop in total energy of the system due to dis-

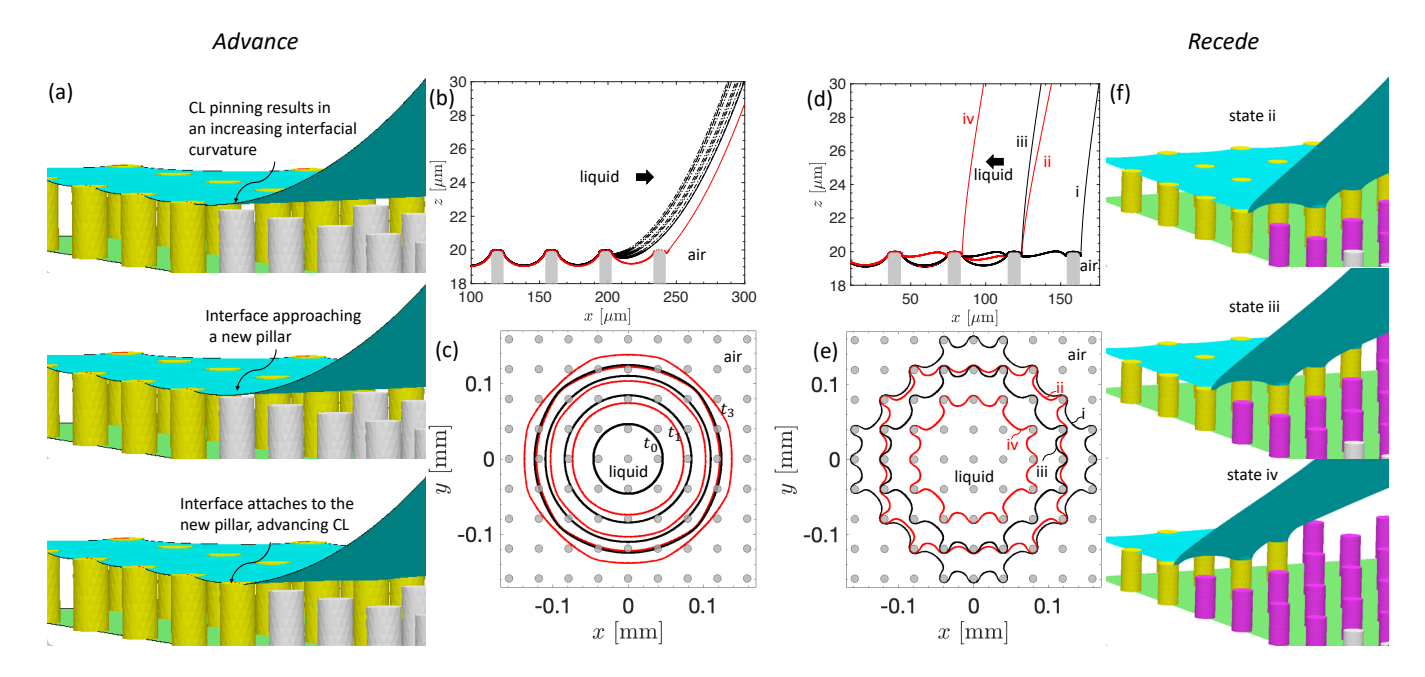


FIG. 3. Depiction of the dynamics of the interface during the advance and recede stages respectively for a 1.6 μ L droplet on a superhydrophobic surface with $\theta_A = 111.2^{\circ}$, $\theta_R = 98.7^{\circ}$ and $\phi = 0.05$. (a) Equilibrium interfacial morphologies showing how the interface advances. The CL stays pinned on a set of pillars while the liquid-air interface curves forward until it contacts the next set of pillars, thereby advancing the CL. The equilibrium interfacial morphologies on the x-z plane is shown in (b). The pinned states are shown by dashed-dotted lines while the equilibrium states just before and after the advancement of the CL are shown by the solid black and solid red lines respectively. (c) Shows the apparent CL measured at a distance of 1 μ m from the pillar tops. The CL starts as a circle (t_0) and eventually acquires a shape resembling that of an octagon as it advances (eg. $t_1 \rightarrow t_3$.) During the recede stage the CL moves in its characteristic stick-slip motion, executing jumps between the first and the second critical states shown by solid back and red lines, respectively, in (d) which shows the equilibrium interfacial morphologies on the x-z plane. The corresponding CL morphologies (at $\Delta z = 1 \mu$ m) are shown in (e). (f) Equilibrium interfacial morphologies corresponding to the critical states ii, iii and iv in (d). The yellow colored pillars indicated pinned pillars, magenta represents the depinned pillars, and the white color represents the pillars which were never contacted by the liquid.

sipation (see Fig. 7 in Appendix B) that results in a small but sharp drop in F, as shown in the insets. A similar sawtooth variation in force during the advancement of CL was observed experimentally by Liimatainen et al. [32]. The advance stage continues until the forces reach a certain maximum value, herein termed the reversal force (F_{rev}) . At this stage, the direction of motion of the disk is reversed and the droplet is pulled away from the surface. It should be noted that the sharp drop in the force observed at the reversal point (shown by dashed lines in the figure) is due to the change in the Young's angle boundary condition at the CL from $\theta_{\rm A}$ to $\theta_{\rm R}$.

During the recede stage, the force magnitude increases (in the opposite direction). The receding motion of the CL is characterized by its typical stick-slip movement that is reflected in a sawtooth variation in the F. The force increases linearly during CL pinning, drops sharply when the CL jumps due to the dissipation of energy (see Fig. 7 in Appendix B), and then increases again linearly when the CL pins again at a new location. The force continues to increase until it reaches a maximum value $F_{\rm max}$, followed by the detachment of the droplet at a relatively lower force $F_{\rm detach}$. The difference between the

distinctive peaks and troughs of the sawtooth variation during the *recede* stage is considerably greater than that during the *advance* stage, because of the higher dissipation of energy during the receding motion as compared to the advancing motion on a superhydrophobic surface.

C. Droplet evaporation

In the above discussion, we showed how the force between a microliter droplet and a pillared superhydrophobic surface varies over time during typical droplet probe microscopy. Up to this point we have assumed that the rate of evaporation of the liquid is negligible and that the droplet volume remains constant during the entire process. However, in reality, if the drop motion is slow enough, then evaporation will cause a change in the droplet volume which may lead to a possible change in the CL dynamics, and subsequently the force. Here, we discuss an alternative approach to measuring the adhesion force between a droplet and the surface that relies on droplet evaporation. The droplet is not pulled away from the surface: instead the disk is kept stationary for

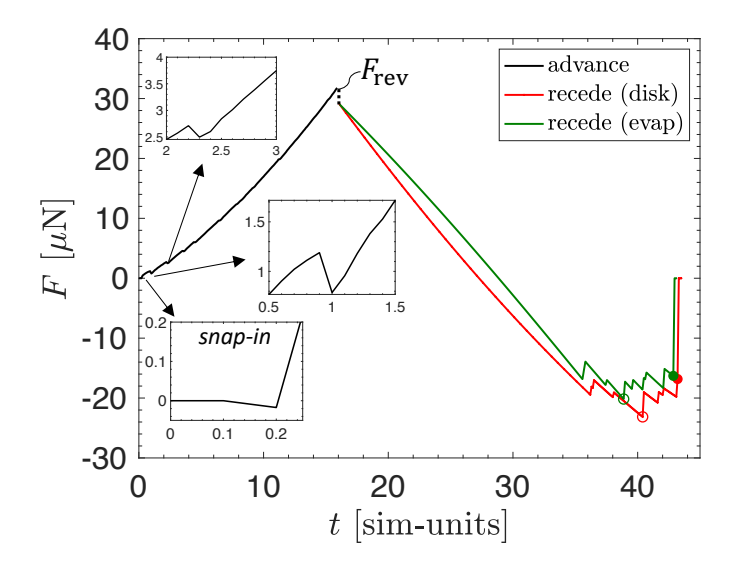


FIG. 4. Variation in the net vertical force F with time t (in simulation units), between a droplet and a superhydrophobic surface during a typical droplet probe microscopy simulation with maximum and detachment forces shown by empty and filled circles respectively. The force variation for the recede stage is shown for both the moving disk (in red) and evaporation (in green) modes. The simulation time for the evaporation mode is scaled down to fit in the same plot. Inset shows the sharp drop in the force during snap-in and two CL advancement moments. The maximum and detachment forces obtained by each approach are comparable. The force curves were generated for a 1.6 μ L droplet on a surface with $\theta_A = 111.2^{\circ}$, $\theta_R = 98.7^{\circ}$ and $\phi = 0.05$.

the entire duration of the recede stage and the droplet is allowed to evaporate, as done for example by Liimatainen et al. [32]. Due to evaporation, the principal radii of curvature of the droplet decrease, resulting in an increase in Laplace pressure (see Fig. S3 in the Supplemental Material). As the size of the droplet reduces, the CL depins from the pillars and jumps to a new equilibrium position, similar to what we observed when the droplet was moved away from the surface. The variation in F during the recede stage is shown in Fig. 4 in green color. Note that the recede stage in the evaporation mode takes much longer compared to the moving disk mode. However, we scaled the simulation time for the evaporation mode to fit both the evaporation and moving disk data in the same plot. For the evaporation mode as well, F varies in a sawtooth manner, reaching a maximum (F_{max}) before the droplet detaches from the surface with a lower force F_{detach} . Compared with the moving disk mode, we observe that both approaches give similar force variations, with $F_{\rm max}$ differing only by a small amount (≈ 3 μ N). Therefore, numerically both approaches are equivalent and, either way, by moving the disk or by letting the droplet evaporate during the recede stage, we will get a similar variation in the net vertical force. Finally, we end this section by commenting that in a typical force tensiometer setup, the droplet weight at the start of the experiment is subtracted, and the tensiometer only measures the interaction force between the droplet and the surface. However, as the droplet evaporates, the change in weight as a result of the loss of mass is not accounted for by the tensiometer, which results in different force curves for evaporation and moving disk modes. This is

discussed in the next section, where we compare the numerical findings with experimental results.

D. Comparison with experiments

In §IVB we discussed the variation in the adhesion force between a droplet and a superhydrophobic surface during a typical droplet probe microscopy. The force curve has a distinct sawtooth variation characterized by the maximum force (F_{max}) and the detachment force (F_{detach}) respectively. Here, we compare the numerical results with the experimental measurements of the adhesion force. In Fig. 5a we show the variation in F with time (s) experimentally measured between a droplet 1.6 μ L in volume and a superhydrophobic surface with $\phi = 0.05, \ \theta_{\rm A} = 111.2^{\circ} \ {\rm and} \ \theta_{\rm R} = 98.7^{\circ} \ [1].$ We also plot the force variation obtained by numerical simulations. Since the numerical simulations only calculate the equilibrium interfacial morphologies, a pseudo time is obtained by assuming a certain velocity for the movement of the disk during the recede stage such that the initial slope of both the curves at the start of the recede stage is matched. We observe a good agreement between the experimental and simulation results, giving confidence that the numerical model is capable of accurately predicting the maximum adhesion force (F_{max}) , which is a characteristic of the surface (discussed in [1]). An important point to note here is that a typical commercial force tensiometer is not capable of capturing the peaks and troughs of the force variation during the recede stage because of limited sensitivity. This would require a much

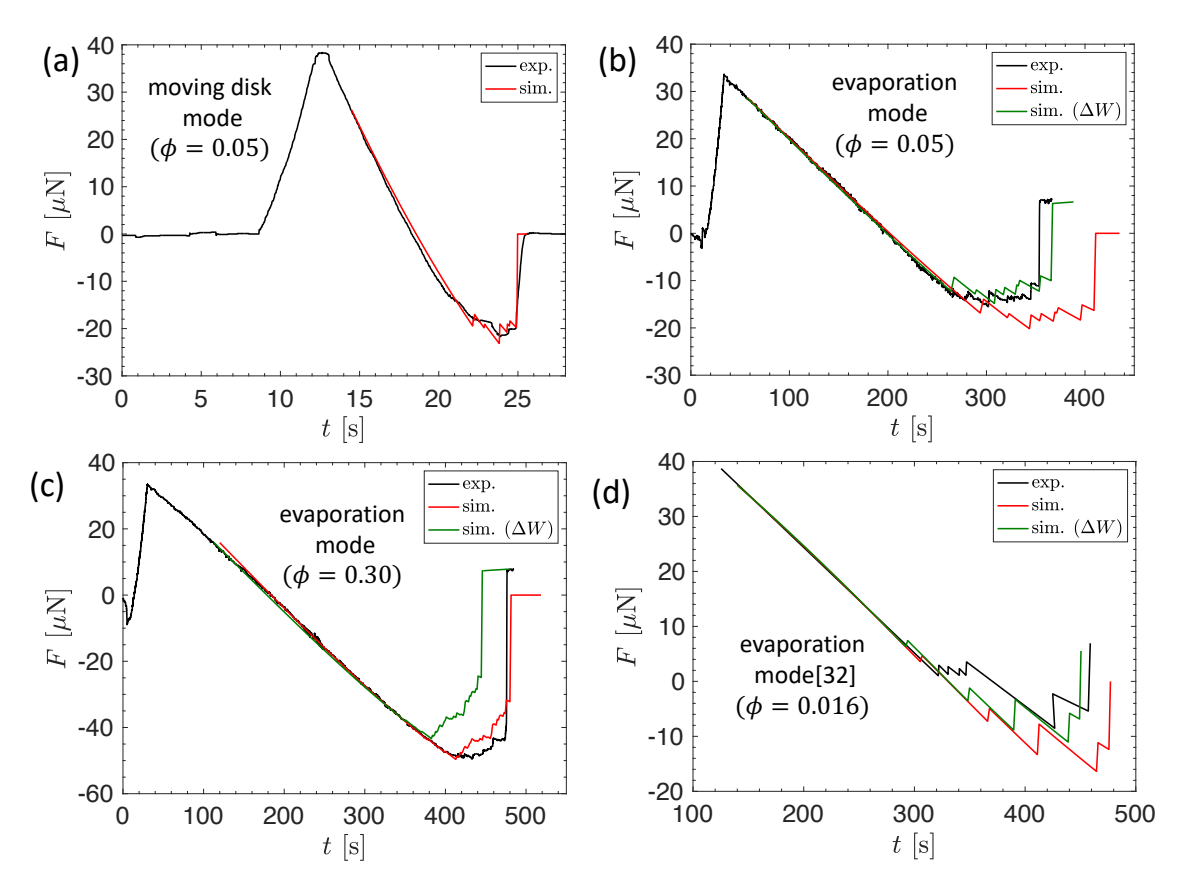


FIG. 5. Variation in the net vertical force (F, in micronewtons) with time (t, in seconds) measured experimentally and calculated via energy minimization simulations. For both the moving disk and evaporation modes, simulation time is scaled linearly to match the initial slope of the experimental force curve during the recede stage. F vs t for a droplet of volume $V=1.6~\mu L$ and a superhydrophobic surface with $\theta_A=111.2^\circ$, $\theta_R=98.7^\circ$ and pillar area fractions $\phi=0.05$ and $\phi=0.30$ are shown in (b) and (c) respectively. The force variation with an additional term for the loss in droplet weight due to evaporation (i.e. $F+\Delta W$) is also plotted in green in (b) and (c). (d) F vs t variation from Liimatainen et al.[32] (in black) and simulation results for the evaporation mode considering change in droplet weight (in green) and without considering change in droplet weight (in red) due to evaporation. The droplet has an initial volume of $V=1.5~\mu L$ and the surface has $\theta_A=111.0^\circ$, $\theta_R=85.1^\circ$ and $\phi=0.016$.

more sensitive tensiometer setup such as the one recently developed by Liimatainen et al. [32]. However, the numerical model presented here is capable of resolving the small force variations and can complement the results obtained using any commercial force tensiometer. In addition, as discussed in [1], only an average of the adhesion forces measured during the recede stage is required to characterize a superhydrophobic surface. Therefore, although a commercial force tensiometer may not be able to resolve all the force peaks, it can still be used to characterize a superhydrophobic surface when complemented by the numerical model (see [1] for details).

Now we compare the numerical results against the experimental data for the case of an evaporating droplet. In Fig. 5b we show the variation in F with time measured experimentally (in black) for an evaporating droplet of an initial volume, $V=1.6~\mu\mathrm{L}$ placed on a superhydrophobic surface with $\phi=0.05,~\theta_\mathrm{A}=111.2^\circ$ and $\theta_\mathrm{R}=98.7^\circ$. The droplet is kept stationary during the entire recede stage

(experimentally, this was achieved by keeping the stage on which the surface was placed stationary). The first difference between the moving disk (or stage in the experiments) and evaporating droplet modes is the duration of the recede stage, which is significantly greater for the latter. For example, for an area fraction of $\phi = 0.05$ the recede stage lasts approximately 300 s during the evaporation mode compared to approximately 10 s during the moving disk mode. This time duration increases even more as the pillar area fraction increases (see Fig. 5c). Another important difference is that, during the evaporation mode, the tensiometer captures some of the peaks and troughs of sawtooth variation in F with time during the recede stage. This is due to a much slower rate of CL motion during the *recede* stage in the evaporation mode. It may appear that by letting the droplet evaporate, a commercial tensiometer can be used to capture the variation in the adhesion force between the surface and the droplet. However, careful observation reveals that loss

of droplet mass as a result of evaporation results in a slight reduction in the measured adhesion force, as seen by a non-zero residual force in Figs. 5b and c after the droplet has detached from the surface. The magnitude of this residual force ($\approx 7.0 \mu N$ in the particular case shown in Fig. 5b) is similar to the change in the weight of the droplet due to evaporation. As an example, in Fig. 8a in Appendix C we show the variation in F with the change in droplet volume (ΔV) obtained numerically $(\phi = 0.05, \theta_A = 111.2^{\circ} \text{ and } \theta_R = 98.7^{\circ})$. We observe that droplet detachment occurs at $\Delta V = 0.64 \ \mu L$, which is equivalent to a weight of 6.26 μ N. The similar magnitudes of the change in droplet weight due to evaporation and the residual force after detachment during the experiments (evaporation mode) suggests that the unaccounted droplet weight may be causing the difference between the experimental and simulation results. To address this, we adjusted the numerically calculated adhesion force by accounting for the equivalent weight of the evaporated droplet mass ΔW at each equilibrium position, shown in green in Fig. 5b (see Appendix C for details regarding mapping of simulation data onto the experimental force curve). We observe that the adjusted force $(F + \Delta W)$ obtained numerically is in good agreement with the experimental data, but not at higher area fractions (Fig. 5c). This may be because the volume of the droplet at the start of the recede stage is unknown. The numerical simulations assume that the advance stage is fast enough so that the loss of vapor as a result of evaporation is negligible. However, there may still be some loss of volume and the droplet may have a different volume at the start of the recede stage compared to the volume at the start of the experiment (or simulation). Finally, we compare the numerical model with the experimental data of Liimatainen et al. [32]. We numerically calculated the adhesion force between a 1.5 μ L droplet (initial volume) and a superhydrophobic surface with $\phi = 0.016$, $\theta_{\rm A}=111.0^{\circ}$ and $\theta_{\rm R}=85.1^{\circ}$. The simulations were performed in the evaporation mode. In Fig. 5d we show the experimental results in black and simulation data in red and green (considering the loss in droplet mass). We observe that the numerical model overpredicts the force, however there is good agreement between model and experiment when taking the loss in droplet mass $(F + \Delta W)$ into account as the measurement proceeds.

Although the numerical model can account for the change in the droplet weight due to evaporation, in reality, there are other factors that may need to be considered. For example, the evaporating droplet can result in a non-uniform change in the surface temperature of the droplet, generating surface tension gradients [92] affecting the variation of the force. In addition, vapor accumulation near the CL can affect the CL pinning by exerting a localized pressure force, resulting in a different variation in the force as the droplet evaporates. Because both of these effects were not incorporated into the numerical model, a complete understanding of the effect of droplet evaporation requires a series of experiments un-

der controlled evaporation, which is outside the scope of this work and will be considered in the future.

V. CONCLUSION

We have presented a novel numerical method to simulate typical droplet probe microscopy on superhydrophobic surfaces composed of periodic pillar structures. The present model can predict the variation in the adhesion force as the different stages of droplet probe microscopy, namely, approach, snap-in, advance, recede, and detach, are performed. The model is suitable for any droplet size, pillar geometry, inter-pillar and surface chemistry (Young's angle), as long as a Cassie-Baxter wetting state can be achieved. The numerical model is also suitable for studying the contact line dynamics, microscale interface dynamics, and variation in the advancing and receding contact angle along the droplet perimeter.

Based on the numerical model, we simulate droplet probe microscopy with a microliter droplet (V = 1.6) μL) and a superhydrophobic surface ($\theta_A = 111.2^{\circ}, \theta_R =$ 98.7°) with cylindrical pillars (height 20 μ m and diameter of 10 μ m). We observe that the adhesion force between the droplet and the surface varies in a sawtooth manner as the droplet contacts the surface, is compressed between the stationary surface and the moving disk, and then is pulled away from the surface by moving the disk in the opposite direction. We observe that the peaks and troughs in this sawtooth variation occur at the moments when the contact line executes a jump and comes to an equilibrium state after executing a jump, respectively. During the recede stage, the adhesion force reaches a maximum before the droplet detaches from the surface at a much lower force magnitude. We simulated a pure evaporation in which both the surface and the disk are not moved during the recede stage, and the droplet is allowed to evaporate, triggering the detachment. We observe that the variation in the force during the recede stage is similar to the case when the disk is moved and the evaporation is not considered. We compared our model with the experimental data of [1] and observed a good agreement for the non-evaporating case. For the evaporating droplet, we observe that the model over-predicts the forces during the recede stage, which is primarily due to the loss in droplet mass as it evaporates. Because only the initial weight of the droplet is adjusted in the microbalance reading, the difference in weight owing to evaporation remains unaccounted for in the experimental measurements. In addition to this, the presence of surface tension gradients as a result of changes in temperature upon evaporation and the localized vapor accumulation near the contact line may also affect the experimental measurements. We also studied the contact line dynamics during the advance and recede stages and observed that the apparent contact line evolves from a circular shape to that resembling an octagon during the advance stage and then goes back to its original circular shape during the *recede* stage. The reason for this interaction of the contact line is the anisotropy in the dissipation of energy during the contact line dynamics, which is left for future work.

This work will help advance direct force measurement technology and has potential for many future studies. The present model can be used to study the stability of the Cassie-Baxter wetting state and the onset of the wetting transition to the Wenzel state. In this work, a single pillar area fraction and a single set of advancing and receding contact angles were considered. It would be interesting to see the effect of a variation in the area fraction of the pillar, the advancing and receding contact angles, and the shape and aspect ratio of the pillars. As an application of the present model, we have presented a methodology for the quantitative characterization of superhydrophobic surfaces using droplet probe microscopy in [1].

ACKNOWLEDGMENTS

J.D.B. received support from an Australian Research Council Future Fellowship (FT220100319) funded by the Australian Government. The authors would like to thank Professor Marta Krasowska from the University of South Australia for her generous support during the experimental part of this study.

Appendix A: Evolution of the apparent CL at $\Delta z = 20~\mu\mathrm{m}$

Figs. 6a and b show the evolution of the apparent CL measured at $\Delta z = 20~\mu\mathrm{m}$ from the tops of the pillars during the advance and recede stages, respectively. During the advance stage, the apparent CL maintains a circular shape as the interface moves forward. However, during the recede stage, the apparent CL evolves from a shape resembling that of an octagon to a shape resembling a circle. In fact, the apparent CL also evolves from a circular shape to a shape resembling an octagon during the advance stage but is contained in a zone very close to the pillars (see Fig. 3c where the apparent CL at $\Delta z = 1~\mu\mathrm{m}$ shows this evolution during the advance stage).

Appendix B: Variation in total energy of the droplet

Fig. 7 shows the variation in the total energy of the droplet in μJ (Eq. (5)) during the *advance* and *recede* stages (moving disk mode) with time in simulation units. The total energy changes as the liquid-air and solid-liquid areas change during the coarse of the simulation run. A sudden drop in energy can be observed at locations where the CL moves at capillary velocities, dissipating energy. The energy dissipation also appears as a drop in F, shown in Fig. 4 in the main text.

Appendix C: Mapping simulation data onto experimental force curve for the evaporation mode

To simulate the evaporation mode in Surface Evolver, we calculated the equilibrium droplet morphology for an initial drop volume V_0 , and then reduce the droplet volume by a fixed percentage to calculate the next equilibrium shape, i.e. $\Delta V = -\alpha V$. Assuming that the droplet density is constant and there is a constant concentration gradient driving mass transfer, then the rate of change of the droplet volume is proportional to the instantaneous liquid-air interfacial area (A_{la}) , that is,

$$\frac{dV}{dt} = -\beta A_{\rm la},\tag{C1}$$

where β is a constant depending on the gradient of vapor concentration, the diffusion coefficient and the droplet density. From the simulation results (Fig. 8), we observe that the interfacial area scales linearly with the droplet volume, $A_{\text{la}} \propto -V$, giving:

$$\frac{dV}{dt} = \beta' V. \tag{C2}$$

Here β' is the new constant of proportionality that includes the area-volume scaling.

The relationship between the change in volume and the change in time can then be written as:

$$\Delta t = \frac{\Delta V}{\beta' V} = \frac{\alpha}{\beta'} = C, \tag{C3}$$

where C is a constant.

To plot the simulation data with the experimentally measured force values, we choose a suitable value of the constant C by scaling the simulation time so that the initial slope of the curve F versus t during the start of the recede stage is the same for both the experimental and the simulation data. This approach does not change to force magnitude or the relative position of different peaks and troughs in the sawtooth variation of the force.

^[1] P. Kumar, M. Krasowska, and J. D. Berry, Probing superhydrophobic surface topography using droplet adhesion

^{(2025),} arXiv:2511.19908 [physics.flu-dyn].

^[2] W. Barthlott and C. Neinhuis, Purity of the sacred lo-

- tus, or escape from contamination in biological surfaces, Planta ${\bf 202}, 1 \ (1997).$
- [3] B. Bhushan and Y. C. Jung, Natural and biomimetic artificial surfaces for superhydrophobicity, self-cleaning, low adhesion, and drag reduction, Progress in Materials Science 56, 1 (2011).
- [4] S. Nishimoto and B. Bhushan, Bioinspired self-cleaning surfaces with superhydrophobicity, superoleophobicity, and superhydrophilicity, RSC Advances 3, 671 (2013).
- [5] L. Feng, Y. Zhang, J. Xi, Y. Zhu, N. Wang, F. Xia, and L. Jiang, Petal effect: a superhydrophobic state with high adhesive force, Langmuir 24, 4114 (2008).
- [6] Y. Jiang, Y. Xiao, and C. Wei, Sticky superhydrophobic state, The Journal of Physical Chemistry Letters 15, 11896 (2024).
- [7] U. Manna and D. M. Lynn, Fabrication of liquid-infused surfaces using reactive polymer multilayers: principles for manipulating the behaviors and mobilities of aqueous fluids on slippery liquid interfaces, Advanced Materials 27, 3007 (2015).
- [8] S. Peppou-Chapman, J. K. Hong, A. Waterhouse, and C. Neto, Life and death of liquid-infused surfaces: a review on the choice, analysis and fate of the infused liquid layer, Chemical Society Reviews 49, 3688 (2020).
- [9] S. Farhadi, M. Farzaneh, and S. A. Kulinich, Anti-icing performance of superhydrophobic surfaces, Applied Surface Science 257, 6264 (2011).
- [10] M. J. Kreder, J. Alvarenga, P. Kim, and J. Aizenberg, Design of anti-icing surfaces: smooth, textured or slippery?, Nature Reviews Materials 1, 1 (2016).
- [11] S. Amini, S. Kolle, L. Petrone, O. Ahanotu, S. Sunny, C. N. Sutanto, S. Hoon, L. Cohen, J. C. Weaver, J. Aizenberg, et al., Preventing mussel adhesion using lubricantinfused materials, Science 357, 668 (2017).
- [12] S. Sunny, G. Cheng, D. Daniel, P. Lo, S. Ochoa, C. Howell, N. Vogel, A. Majid, and J. Aizenberg, Transparent antifouling material for improved operative field visibility in endoscopy, Proceedings of the National Academy of Sciences 113, 11676 (2016).
- [13] L. Bocquet and E. Lauga, A smooth future?, Nature Materials 10, 334 (2011).
- [14] M. Xu, A. Grabowski, N. Yu, G. Kerezyte, J.-W. Lee, B. R. Pfeifer, and C.-J. Kim, Superhydrophobic drag reduction for turbulent flows in open water, Physical Review Applied 13, 034056 (2020).
- [15] S. Zhang, J. Huang, Z. Chen, S. Yang, and Y. Lai, Liquid mobility on superwettable surfaces for applications in energy and the environment, Journal of Materials Chemistry A 7, 38 (2019).
- [16] H. Li, W. Fang, Y. Li, Q. Yang, M. Li, Q. Li, X.-Q. Feng, and Y. Song, Spontaneous droplets gyrating via asymmetric self-splitting on heterogeneous surfaces, Nature Communications 10, 950 (2019).
- [17] J. C. Bird, R. Dhiman, H.-M. Kwon, and K. K. Varanasi, Reducing the contact time of a bouncing drop, Nature 503, 385 (2013).
- [18] M. Villegas, Y. Zhang, N. Abu Jarad, L. Soleymani, and T. F. Didar, Liquid-infused surfaces: a review of theory, design, and applications, Acs Nano 13, 8517 (2019).
- [19] D. Quéré, Non-sticking drops, Reports on Progress in Physics 68, 2495 (2005).
- [20] P. Roach, N. J. Shirtcliffe, and M. I. Newton, Progess in superhydrophobic surface development, Soft Matter 4, 224 (2008).

- [21] D. Daniel, M. Vuckovac, M. Backholm, M. Latikka, R. Karyappa, X. Q. Koh, J. V. I. Timonen, N. Tomczak, and R. H. A. Ras, Probing surface wetting across multiple force, length and time scales, Communications Physics 6, 152 (2023).
- [22] L. Wang and T. J. McCarthy, Covalently attached liquids: instant omniphobic surfaces with unprecedented repellency, Angewandte Chemie International Edition 55, 244 (2016).
- [23] C. Furmidge, Studies at phase interfaces. i. the sliding of liquid drops on solid surfaces and a theory for spray retention, Journal of Colloid Science 17, 309 (1962).
- [24] Y. Stern, R. Tadmor, A. Miron, and A. Vinod, Furmidge equation revisited, Langmuir 41, 11785 (2025).
- [25] G. McHale, N. Gao, G. G. Wells, H. Barrio-Zhang, and R. Ledesma-Aguilar, Friction coefficients for droplets on solids: The liquid–solid amontons' laws, Langmuir 38, 4425 (2022).
- [26] N. Gao, F. Geyer, D. W. Pilat, S. Wooh, D. Vollmer, H.-J. Butt, and R. Berger, How drops start sliding over solid surfaces, Nature Physics 14, 191 (2018).
- [27] D. Daniel, M. Vuckovac, M. Backholm, M. Latikka, R. Karyappa, X. Q. Koh, J. V. Timonen, N. Tomczak, and R. H. Ras, Probing surface wetting across multiple force, length and time scales, Communications Physics 6, 152 (2023).
- [28] T. P. Allred, J. A. Weibel, and S. V. Garimella, A wettability metric for characterization of capillary flow on textured superhydrophilic surfaces, Langmuir 33, 7847 (2017).
- [29] T. Huhtamäki, X. Tian, J. T. Korhonen, and R. H. Ras, Surface-wetting characterization using contactangle measurements, Nature Protocols 13, 1521 (2018).
- [30] D. Daniel, C. L. Lay, A. Sng, C. J. Jun Lee, D. C. Jin Neo, X. Y. Ling, and N. Tomczak, Mapping micrometer-scale wetting properties of superhydrophobic surfaces, Proceedings of the National Academy of Sciences 116, 25008 (2019), publisher: Proceedings of the National Academy of Sciences.
- [31] D. Daniel, Y. Florida, C. L. Lay, X. Q. Koh, A. Sng, and N. Tomczak, Quantifying Surface Wetting Properties Using Droplet Probe Atomic Force Microscopy, ACS Applied Materials & Interfaces 12, 42386 (2020).
- [32] V. Liimatainen, M. Vuckovac, V. Jokinen, V. Sariola, M. J. Hokkanen, Q. Zhou, and R. H. Ras, Mapping microscale wetting variations on biological and synthetic water-repellent surfaces, Nature Communications 8, 1798 (2017).
- [33] M. J. Hokkanen, M. Backholm, M. Vuckovac, Q. Zhou, and R. H. A. Ras, Force-Based Wetting Characterization of Stochastic Superhydrophobic Coatings at Nanonewton Sensitivity, Advanced Materials 33, 2105130 (2021).
- [34] D. W. Pilat, P. Papadopoulos, D. Schäffel, D. Vollmer, R. Berger, and H.-J. Butt, Dynamic Measurement of the Force Required to Move a Liquid Drop on a Solid Surface, Langmuir 28, 16812 (2012).
- [35] N. Gao, F. Geyer, D. W. Pilat, S. Wooh, D. Vollmer, H.-J. Butt, and R. Berger, How drops start sliding over solid surfaces, Nature Physics 14, 191 (2018).
- [36] C. Shi, X. Cui, L. Xie, Q. Liu, D. Y. C. Chan, J. N. Israelachvili, and H. Zeng, Measuring Forces and Spatiotemporal Evolution of Thin Water Films between an Air Bubble and Solid Surfaces of Different Hydrophobicity, ACS Nano 9, 95 (2015).

- [37] D. Daniel, J. V. Timonen, R. Li, S. J. Velling, and J. Aizenberg, Oleoplaning droplets on lubricated surfaces, Nature Physics 13, 1020 (2017).
- [38] D. Daniel, A. Y. T. Chia, L. C. H. Moh, R. Liu, X. Q. Koh, X. Zhang, and N. Tomczak, Hydration lubrication of polyzwitterionic brushes leads to nearly friction-and adhesion-free droplet motion, Communications Physics 2, 105 (2019).
- [39] M. Backholm, D. Molpeceres, M. Vuckovac, H. Nurmi, M. J. Hokkanen, V. Jokinen, J. V. Timonen, and R. H. Ras, Water droplet friction and rolling dynamics on superhydrophobic surfaces, Communications Materials 1, 64 (2020).
- [40] C. Hinduja, A. Laroche, S. Shumaly, Y. Wang, D. Vollmer, H.-J. Butt, and R. Berger, Scanning drop friction force microscopy, Langmuir 38, 14635 (2022).
- [41] C. Shi, X. Cui, L. Xie, Q. Liu, D. Y. Chan, J. N. Israelachvili, and H. Zeng, Measuring forces and spatiotemporal evolution of thin water films between an air bubble and solid surfaces of different hydrophobicity, ACS Nano 9, 95 (2015).
- [42] C. Shi, B. Yan, L. Xie, L. Zhang, J. Wang, A. Takahara, and H. Zeng, Long-range hydrophilic attraction between water and polyelectrolyte surfaces in oil, Angewandte Chemie International Edition 55, 15017 (2016).
- [43] B. Samuel, H. Zhao, and K.-Y. Law, Study of wetting and adhesion interactions between water and various polymer and superhydrophobic surfaces, The Journal of Physical Chemistry C 115, 14852 (2011).
- [44] G. Livi, F. Fazal, H. Barrio-Zhang, H. Zhao, G. McHale, G. G. Wells, A. Syed, N. Radacsi, and V. Koutsos, Characterization of water adhesion of pcl and plcl electrospun fiber mats and their correlation to wettability, Macromolecular Materials and Engineering, e00189 (2025).
- [45] S. Lepikko, V. Turkki, T. Koskinen, R. Raju, V. Jokinen, M. S. Kiseleva, S. Rantataro, J. V. Timonen, M. Backholm, I. Tittonen, et al., Droplet friction on superhydrophobic surfaces scales with liquid-solid contact fraction, Small 21, 2405335 (2025).
- [46] M. Backholm, T. Kärki, H. A. Nurmi, M. Vuckovac, V. Turkki, S. Lepikko, V. Jokinen, D. Quéré, J. V. Timonen, and R. H. Ras, Toward vanishing droplet friction on repellent surfaces, Proceedings of the National Academy of Sciences 121, e2315214121 (2024).
- [47] N. Nagy, Determination of solid-liquid adhesion work on flat surfaces in a direct and absolute manner, Scientific Reports 14, 29991 (2024).
- [48] Z. Dong, M. F. Schumann, M. J. Hokkanen, B. Chang, A. Welle, Q. Zhou, R. H. Ras, Z. Xu, M. Wegener, and P. A. Levkin, Superoleophobic slippery lubricant-infused surfaces: combining two extremes in the same surface, Advanced Materials 30, 1803890 (2018).
- [49] D. Öner and T. J. McCarthy, Ultrahydrophobic surfaces. effects of topography length scales on wettability, Langmuir 16, 7777 (2000).
- [50] C. Priest, R. Sedev, and J. Ralston, Asymmetric wetting hysteresis on chemical defects, Physical Review Letters 99, 026103 (2007).
- [51] W. Choi, A. Tuteja, J. M. Mabry, R. E. Cohen, and G. H. McKinley, A modified cassie-baxter relationship to explain contact angle hysteresis and anisotropy on nonwetting textured surfaces, Journal of Colloid and Interface Science 339, 208 (2009).

- [52] C. Dorrer and J. Rühe, Contact line shape on ultrahydrophobic post surfaces, Langmuir 23, 3179 (2007).
- [53] A. Gauthier, M. Rivetti, J. Teisseire, and E. Barthel, Role of kinks in the dynamics of contact lines receding on superhydrophobic surfaces, Physical Review Letters 110, 046101 (2013).
- [54] C. Dorrer and J. Rühe, Advancing and receding motion of droplets on ultrahydrophobic post surfaces, Langmuir 22, 7652 (2006).
- [55] S. Iliev and N. Pesheva, Contact-angle hysteresis on periodic microtextured surfaces: Strongly corrugated liquid interfaces, Physical Review E 93, 062801 (2016).
- [56] H. Kusumaatmaja and J. Yeomans, Modeling contact angle hysteresis on chemically patterned and superhydrophobic surfaces, Langmuir 23, 6019 (2007).
- [57] M. Rivetti, J. Teisseire, and E. Barthel, Surface fraction dependence of contact angles induced by kinks in the triple line, Physical Review Letters 115, 016101 (2015).
- [58] B. M. Mognetti and J. Yeomans, Modeling receding contact lines on superhydrophobic surfaces, Langmuir 26, 18162 (2010).
- [59] C. Priest, T. W. Albrecht, R. Sedev, and J. Ralston, Asymmetric wetting hysteresis on hydrophobic microstructured surfaces, Langmuir 25, 5655 (2009).
- [60] M. Reyssat and D. Quéré, Contact angle hysteresis generated by strong dilute defects, The Journal of Physical Chemistry B 113, 3906 (2009).
- [61] K.-Y. Yeh, L.-J. Chen, and J.-Y. Chang, Contact angle hysteresis on regular pillar-like hydrophobic surfaces, Langmuir 24, 245 (2008).
- [62] Y. Kwon, S. Choi, N. Anantharaju, J. Lee, M. Panchagnula, and N. Patankar, Is the cassie- baxter formula relevant?, Langmuir 26, 17528 (2010).
- [63] F. Schellenberger, N. Encinas, D. Vollmer, and H.-J. Butt, How water advances on superhydrophobic surfaces, Physical Review Letters 116, 096101 (2016).
- [64] H.-J. Butt, Capillary forces: Influence of roughness and heterogeneity, Langmuir 24, 4715 (2008).
- [65] J.-C. Baret and M. Brinkmann, Wettability control of droplet deposition and detachment, Physical Review Letters 96, 146106 (2006).
- [66] D. Daniel and X. Q. Koh, Droplet detachment force and its relation to young-dupre adhesion, Soft Matter 19, 8434 (2023).
- [67] M. S. Sadullah, Y. Xu, S. Arunachalam, and H. Mishra, Predicting droplet detachment force: Young-dupré model fails, young-laplace model prevails, Communications Physics 7, 89 (2024).
- [68] R. Tadmor, L. Dang, A. Leh, P. Bahadur, and K. Chaurasia, Centrifugal adhesion balance (CAB): A novel surface characterization technique, in APS March Meeting Abstracts (2008) pp. Q22–013.
- [69] S. Chen, B. Zhang, X. Gao, Z. Liu, and X. Zhang, Direction dependence of adhesion force for droplets on rough substrates, Langmuir 33, 2472 (2017).
- [70] P. Sudersan, M. Müller, M. Hormozi, S. Li, H.-J. Butt, and M. Kappl, Method to measure surface tension of microdroplets using standard afm cantilever tips, Langmuir 39, 10367 (2023).
- [71] P. Kumar and D. J. E. Harvie, Energy dissipation during wenzel wetting via roughness scale interface dynamics, Langmuir 40, 16190 (2024).
- [72] P. Kumar, P. Mulvaney, and D. J. Harvie, Energy dissipation during homogeneous wetting of surfaces with

- randomly and periodically distributed cylindrical pillars, Journal of Colloid and Interface Science 659, 105 (2024).
- [73] The interfacial tension of the solid-liquid interface between the droplet and the material of the disk will be different from that between the droplet and the pillared surface, but for simplicity both are considered as the same.
- [74] P. G. de Gennes, F. Brochard Wyart, and D. Quéré, Capillarity and wetting phenomena: drops, bubbles, pearls, waves (Springer Science & Business Media, 2003).
- [75] K. A. Brakke, The surface evolver, Experimental Mathematics 1, 141 (1992).
- [76] K. A. Brakke, Surface evolver manual, Mathematics Department, Susquehanna University, Selinsgrove, PA 17870, 291 (2013).
- [77] A. H. Barr, Superquadrics and angle-preserving transformations, IEEE Computer Graphics and Applications 1, 11 (1981).
- [78] J. W. Gibbs, The scientific papers, Vol I: Thermodynamics, Dover Publications (1961).
- [79] D. Dyson, Contact line stability at edges: Comments on gibbs's inequalities, The Physics of Fluids 31, 229 (1988).
- [80] A. T. Paxson and K. K. Varanasi, Self-similarity of contact line depinning from textured surfaces, Nature Communications 4, 1492 (2013).
- [81] L. Gao and T. J. McCarthy, The "lotus effect" explained: two reasons why two length scales of topography are important, Langmuir 22, 2966 (2006).
- [82] C. Dorrer and J. Rühe, Micro to nano: Surface size scale and superhydrophobicity, Beilstein Journal of Nanotechnology 2, 327 (2011).
- [83] Y. H. Yeong, A. Milionis, E. Loth, and I. S. Bayer, Microscopic receding contact line dynamics on pillar and ir-

- regular superhydrophobic surfaces, Scientific Reports 5, 8384 (2015).
- [84] W. S. Wong, T. P. Corrales, A. Naga, P. Baumli, A. Kaltbeitzel, M. Kappl, P. Papadopoulos, D. Vollmer, and H.-J. Butt, Microdroplet contaminants: when and why superamphiphobic surfaces are not self-cleaning, ACS Nano 14, 3836 (2020).
- [85] B. He, J. Lee, and N. A. Patankar, Contact angle hysteresis on rough hydrophobic surfaces, Colloids and Surfaces A: Physicochemical and Engineering Aspects 248, 101 (2004).
- [86] P. Papadopoulos, L. Mammen, X. Deng, D. Vollmer, and H.-J. Butt, How superhydrophobicity breaks down, Proceedings of the National Academy of Sciences 110, 3254 (2013).
- [87] D. J. Harvie, Contact-angle hysteresis on rough surfaces: mechanical energy balance framework, Journal of Fluid Mechanics 986, A17 (2024).
- [88] Y. Jiang, W. Xu, M. A. Sarshar, and C.-H. Choi, Generalized models for advancing and receding contact angles of fakir droplets on pillared and pored surfaces, Journal of Colloid and Interface Science 552, 359 (2019).
- [89] N. A. Patankar, Hysteresis with regard to cassie and wenzel states on superhydrophobic surfaces, Langmuir 26, 7498 (2010).
- [90] T. L. Liu, Z. Chen, and C.-J. Kim, A dynamic cassie—baxter model, Soft Matter 11, 1589 (2015).
- [91] A. F. Smith, K. Mahelona, and S. C. Hendy, Rolling and slipping of droplets on superhydrophobic surfaces, Physical Review E 98, 033113 (2018).
- [92] P. J. Dekker, C. Diddens, M. N. van der Linden, and D. Lohse, Hidden in plain sight: How evaporation impacts the pendant drop method, arXiv preprint arXiv:2508.07349 (2025).

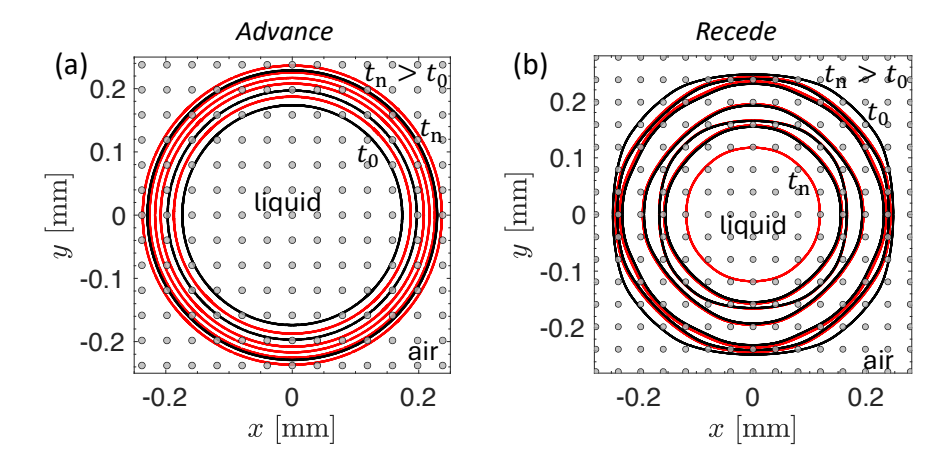


FIG. 6. Evolution of the apparent CL ($\Delta z = 20~\mu\text{m}$) of a droplet of volume ($V = 1.6~\mu\text{L}$) on a superhydrophobic surface with $\theta_{\rm A} = 111.2^{\circ}$, $\theta_{\rm R} = 98.7^{\circ}$ and $\phi = 0.05$ during the (a) advance and (b) recede stages respectively.

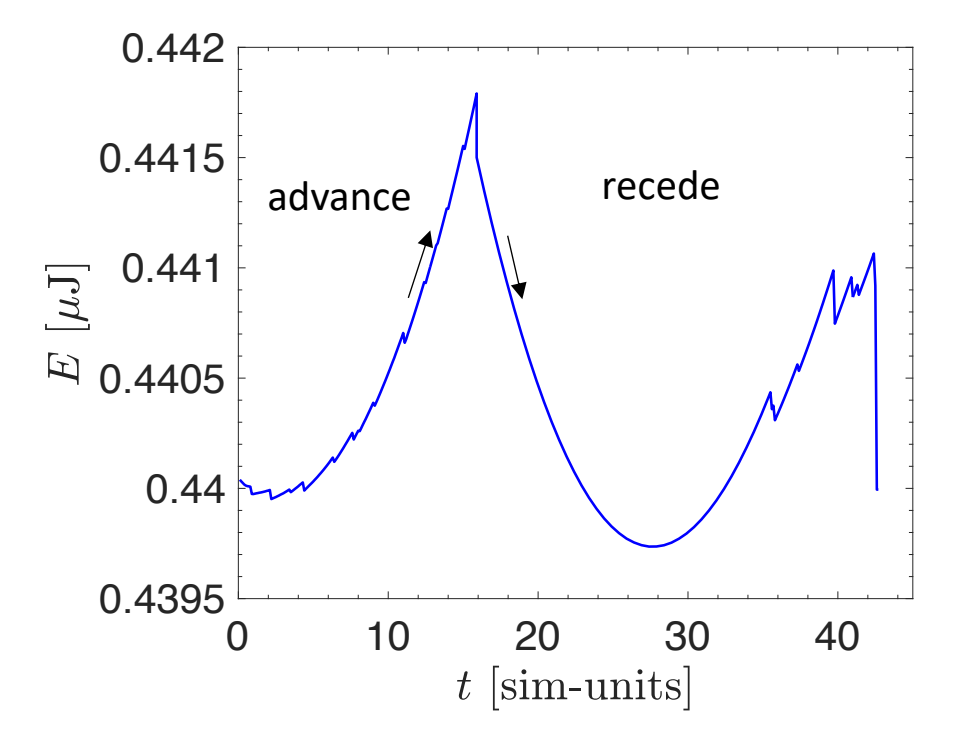


FIG. 7. Variation in total energy in μ J (Eq. (5)) with time in simulation units during the *advance* and *recede* stage of droplet probe microscopy obtained via energy minimization simulations. A droplet of volume $V=1.6~\mu$ L and a superhydrophobic surface with $\theta_{\rm A}=111.2^{\circ}$, $\theta_{\rm R}=98.7^{\circ}$ and $\phi=0.05$ were used in the simulation.

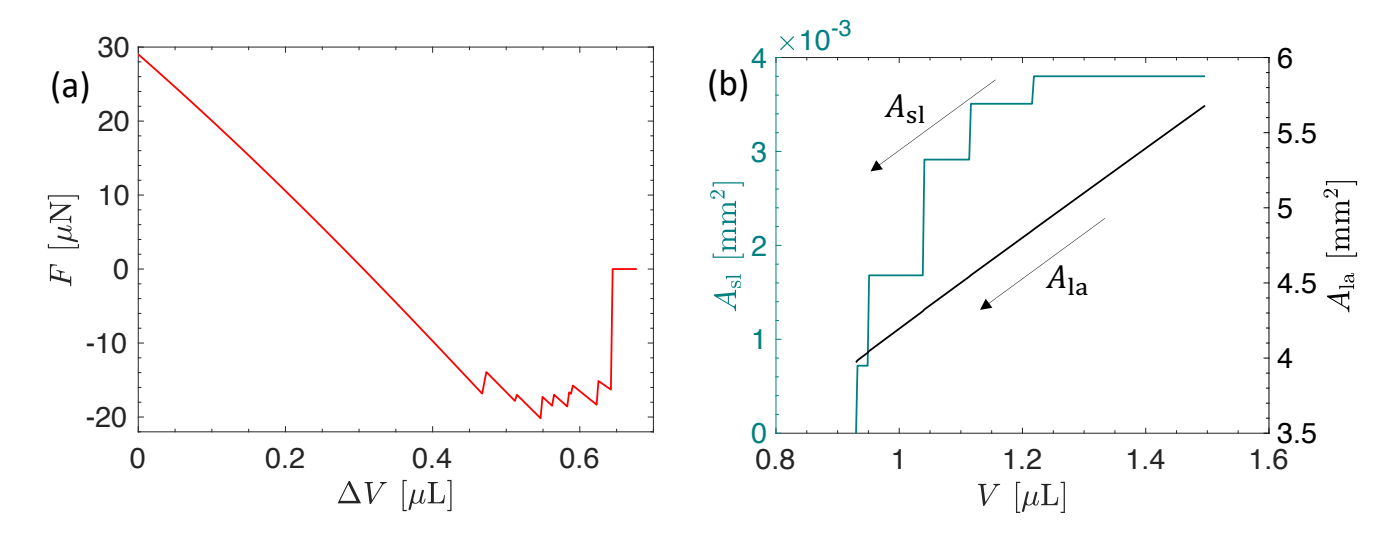


FIG. 8. (a) Simulation results of the variation in the net vertical force with the change in droplet volume during evaporation mode on a superhydrophobic surface with $\theta_{\rm A}=111.2^{\circ}$, $\theta_{\rm R}=98.7^{\circ}$ and $\phi=0.05$. The droplet has an initial volume of V=1.6 $\mu{\rm L}$. (b) Variation in the solid-liquid $(A_{\rm sl})$ and liquid-air $(A_{\rm la})$ interfacial areas during the *recede* stage in evaporation mode on a superhydrophobic surface with $\phi=0.016$, $\theta_{\rm A}=111.0^{\circ}$ and $\theta_{\rm R}=85.1^{\circ}$. The droplet had an initial volume of 1.5 $\mu{\rm L}$ at the start of the *recede* stage. This simulation replicates the experiments of Liimatainen *et al.* [32].